

Strain-engineered high-temperature ferromagnetic Oxygen-substituted NaMnF_3 from first principles

Wen-ning Ren,^{1,2} Kuijuan Jin,^{1,2,3,*} Er-Jia Guo,^{1,2} Chen Ge,^{1,2} Can
Wang,^{1,2,3} Xiulai Xu,^{1,2,3} Hongbao Yao,^{1,2} Litong Jiang,^{1,2} and Guozhen
Yang^{1,2}

¹*Beijing National Laboratory for Condensed Matter Physics, Institute of Physics,
Chinese Academy of Sciences, Beijing 100190, China*

²*School of Physical Sciences, University of Chinese Academy of Sciences, Beijing
100049, China*

³*Songshan Lake Materials Laboratory, Dongguan 523808, China*

* Author to whom correspondence should be addressed to Kuijuan Jin:

kjjin@iphy.ac.cn

Using first-principles calculations, we investigated the magnetic, electronic, and structural properties of oxygen-substituted NaMnF_3 ($\text{NaMnF}_{1.5}\text{O}_{1.5}$) with in-plane biaxial strain. For simplicity, a structure containing an oxygen octahedron is used to explore the underlying physical mechanism. We found that the oxygen octahedron induces a transition from an insulating antiferromagnet to a high-temperature half-metallic ferromagnet. More importantly, the Curie temperature can be significantly enhanced and even might reach room temperature by applying tensile strain. The changing trends of exchange coupling constants with the increasing biaxial tensile strain can be attributed to the cooperative effects of Jahn-Teller distortion and rotation distortion. It is

expected that these findings can enrich the versatility of NaMnF_3 and make it a promising candidate for spintronic applications.

I INTRODUCTION

Intriguing physical phenomena in perovskite materials have been of theoretical and experimental interest, e.g., magnetism [1], ferroelectricity [2,3], multiferroicity [4-6], piezoelectricity [7], and superconductivity [8]. Perovskite oxides are most extensively studied due to exotic physical properties harboring colossal magnetoresistance [9], unconventional superconductivity [10,11], which stems from a complex correlation among electronic, spin, structural, and orbital degrees of freedom [12,13]. In contrast, although some specific properties are demonstrated in halide perovskites [14] such as photocatalytic behavior in KMgF_3 [15] and the phase transition from the perovskite to the postperovskite in NaCoF_3 and NaNiF_3 [16,17], the researches on the magnetic properties for the fluoroperovskite are still scarce and desiderative [18,19].

NaMnF_3 , an incipient multiferroic fluoroperovskite, having a coupling phenomenon of ferroelectricity and G-type antiferromagnetic (G-AFM) ordering with a transition temperature of 66 K from the antiferromagnetic to the paramagnetic state [6,20], has attracted significant interest theoretically [6,21] and experimentally [19,22,23]. Nevertheless, the antiferromagnetic ground state limits the applications of NaMnF_3 in information storage [24,25] and spintronics [26]. So far, the

ferromagnetic property based on NaMnF_3 has never been investigated experimentally or theoretically, let alone the half-metallic ferromagnetism, which is one of the most demanded property for spintronics [27,28]. The previous studies have shown that, unlike oxides, in which the hybridization plays a dominant role, the effective ionic charges in fluoroperovskites are close to their nominal valence [6,21]. Furthermore, it is known that rotations and distortions of the oxygen octahedra affect the magnetic, electrical, and structural functionalities of perovskites [29-31]. Moreover, these properties can be conveniently tailored using external control parameters such as strain [32,33], electric field [34], and pressure [20]. For example, strain-induced magnetism in perovskite oxides was reported both theoretically [13,35] and experimentally [29,36]. Previous studies have also shown that the perovskite oxyfluorides, oxyhydrides, and oxynitrides have been synthesized by topochemical reactions, and novel effects of anion substitution on physical properties such as magnetic coupling [37,38] and dielectric properties [39] have been unveiled. For further exploring some novel property of the fluoroperovskite and establishing a link with perovskite oxides, here, by adopting the method of anion substitution, we theoretically predict a simple structure in which the oxygen octahedra are introduced into NaMnF_3 by replacing half fluorine atoms with oxygen atoms ($\text{NaMnF}_{1.5}\text{O}_{1.5}$), and its novel magnetic and transport properties,

especially manipulated by the in-plane biaxial strain. We speculate that the structure is reasonable in accordance with the previous theoretical result [40], which means that $\text{NaMnF}_{1.5}\text{O}_{1.5}$ should exhibit well-ordered anion configuration due to the low-symmetry features inherited from precursor (NaMnF_3).

Except presenting the results of high-temperature ferromagnetism and electronic structures in $\text{NaMnF}_{1.5}\text{O}_{1.5}$ by employing first-principles calculations, we demonstrate that oxygen octahedron induces a transition from an insulating antiferromagnet to a late-model half-metallic ferromagnet and the Curie temperature (T_C) can be significantly increased by an in-plane biaxial tensile strain. Our results propose a new high-temperature half-metallic ferromagnet and illustrate the ability of strain engineering in tuning magnetism in $\text{NaMnF}_{1.5}\text{O}_{1.5}$.

II COMPUTATIONAL METHOD

The first-principles calculations based on density functional theory (DFT) are performed by Vienna *ab initio* simulation package (VASP) [41,42]. The core and valence electrons are described by projected augmented wave (PAW) [43], with the electronic configuration as follows: $3s^1$ (Na), $3d^64s^1$ (Mn), $2s^22p^5$ (F) and $2s^22p^6$ (O). We apply the generalized gradient approximation (GGA) exchange-correlation interaction within the revised Perdew-Burke-Ernzerhof method for solids (PBEsol) [44]. The GGA+U method [45] is adopted to improve the

description of on-site Coulomb interactions to the Mn d orbital with $U_{\text{eff}} = 4.0$ eV ($U_{\text{eff}} = U - J$, where the Hund exchange parameter J is set to 0 eV.) according to the previous studies [20,46]. Different U_{eff} are also conducted for magnetic ground state (See Fig. S1 in Supplemental Material for details [47]). For structural optimization, the GGA+U is adopted within different magnetic states to perform a full relaxation, including FM, C-AFM, A-AFM, and G-AFM in both NaMnF₃ and NaMnF_{1.5}O_{1.5}. The Fig. S2 [47] shows the effect of U_{eff} on the structural parameters. An 800 eV kinetic energy cutoff of the plane-wave basis set is used for all calculations. The Monkhorst-Pack K-mesh of 6×4×6 is used in the full Brillouin zone. The maximum convergence forces are optimized until less than 0.01 eV/Å, and the convergence criterion for the energy differences is set as 1×10^{-6} eV. The crystal structures in the paper are drawn by VESTA Program [48].

III RESULTS AND DISCUSSION

The side and top views of the orthorhombic perovskite NaMnF₃ with the space group $Pnma$ (No. 62) [49] are shown in Figs. 1(a) and 1(b), respectively, originating from a distortion of the cubic $Pm\bar{3}m$ perovskite. The tilting of the purple MnF₆ octahedra of the $a^-b^+a^-$ type according to the Glazer's labeling [31], the deformation of octahedra, and the displacement of Na⁺ cations result in the change of structural symmetry, indicating the coupling between tilting of MnF₆ and Na⁺ displacement

exists in the orthorhombic structure of NaMnF_3 [6]. We obtained the lattice parameters $a = 5.72 \text{ \AA}$, $b = 7.96 \text{ \AA}$, and $c = 5.49 \text{ \AA}$ from our DFT calculations, the corresponding accuracy is 99.46%, 99.41%, and 99%, respectively, compared with the experimental data [50]. Figures 1(c) and 1(d) show the side and top views of $\text{NaMnF}_{1.5}\text{O}_{1.5}$ with space group $\text{P}\bar{1}$ (No. 2), respectively, by substituting fluorine atoms with oxygen atoms and introducing the oxygen octahedra into NaMnF_3 . The detailed results are listed in Table I, where the lattice constants of $\text{NaMnF}_{1.5}\text{O}_{1.5}$ are smaller in analogy to the intrinsic NaMnF_3 due to the role of hybridization in oxide perovskites [51]. Four possible structures based on the position of MnO_6 octahedron in $\text{NaMnF}_{1.5}\text{O}_{1.5}$ are shown in Fig. S3 [47], while no significant variations of the lattice parameters, energy difference for the different magnetic states, or total energy for the ground state are observed, some details are listed in Table. S1 [47]. The density of states (DOSs) of four structures are basically the same, as shown in Fig. S4 [47]. Then, the formation energy E_{for} of $\text{NaMnF}_{1.5}\text{O}_{1.5}$ is calculated to study the thermodynamical stability [52,53], which can be evaluated by the following expression:

$$E_{for} = E(\text{NaMnF}_{1.5}\text{O}_{1.5}) - E(\text{NaMnF}_3) - \frac{3}{2} E(\text{O}) + \frac{3}{2} E(\text{F}), \quad (1)$$

where $E(\text{NaMnF}_{1.5}\text{O}_{1.5})$ and $E(\text{NaMnF}_3)$ are the total energies of $\text{NaMnF}_{1.5}\text{O}_{1.5}$ and NaMnF_3 , respectively. $E(\text{O}) = \frac{1}{2}E_{\text{O}_2}$ and $E(\text{F}) =$

$\frac{1}{2}E_{F_2}$, where the E_{O_2} and E_{F_2} denote the energies of oxygen and fluorine molecules, respectively. The negative formation energy -2.51 eV indicates the perovskite oxyfluoride is experimentally feasible [53-56].

Furthermore, the tolerance factor t is usually used as a descriptor for the stability of perovskite structure [57,58]. For the perovskite oxyfluorides $\text{NaMnF}_{1.5}\text{O}_{1.5}$, it is defined as

$$t = \frac{r_A + r_C}{\sqrt{2}(r_B + r_C)}, \quad (2)$$

where r_A (1.02 Å), r_B , and r_C are the ionic radii of the Na^+ , the arithmetic average radii of coexisting Mn^{3+} (0.65 Å) and Mn^{2+} (0.67 Å), and the weighted average of two anion radii, respectively. Here,

$$r_C = x \cdot r_{O^{2-}} + (1 - x) \cdot r_{F^-}, \quad (3)$$

with x denoting the fraction of oxygen, $r_{O^{2-}}=1.40$ Å, and $r_{F^-}=1.33$ Å. We calculate the value for $t = 0.83$, implying the perovskite structure can be maintained.

To determine the relative stability between different magnetic states, four possible spin orderings are considered: FM, C-AFM, A-AFM, and G-AFM (see Fig. 2). The energy difference between different magnetic configurations indicates a phase transition from G-AFM-state NaMnF_3 to FM-state $\text{NaMnF}_{1.5}\text{O}_{1.5}$, and the $\text{NaMnF}_{1.5}\text{O}_{1.5}$ possesses high magnetic moments, as shown in Table I.

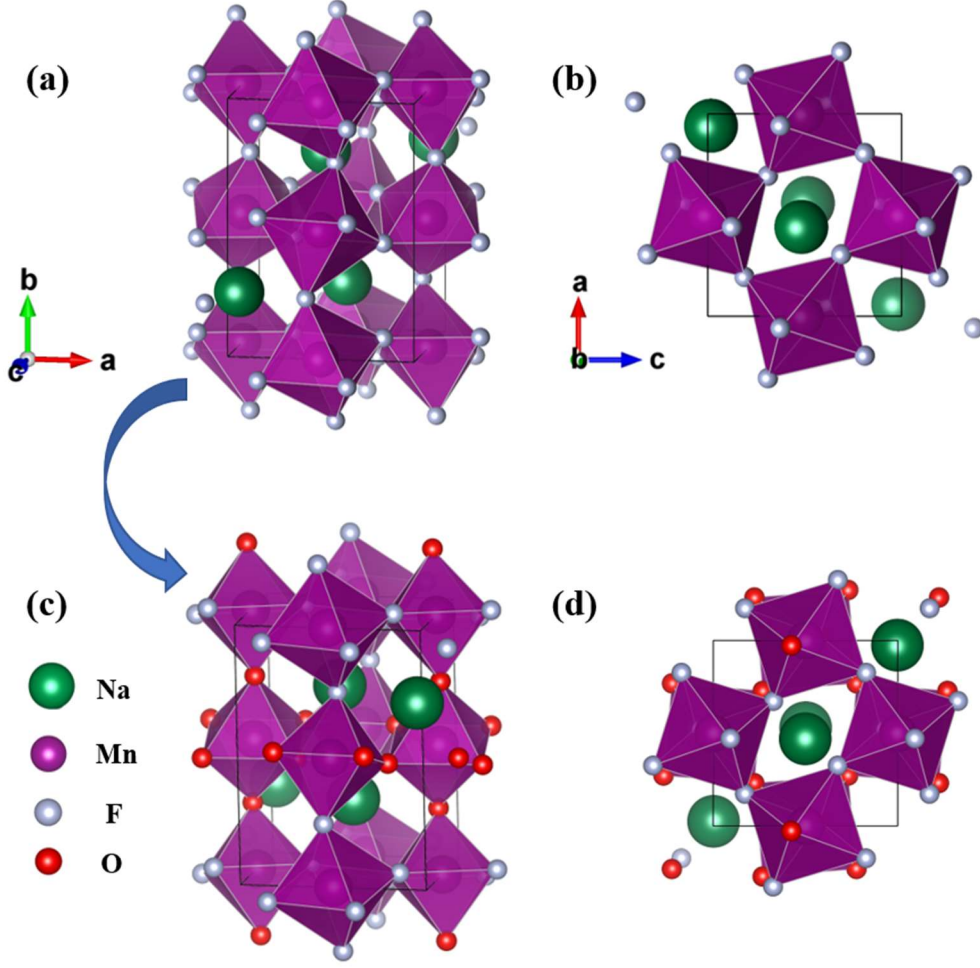


FIG. 1. Crystalline structures. (a) Side and (b) top views of orthorhombic perovskite NaMnF_3 ($Pnma$). (c) Side and (d) top views of $\text{NaMnF}_{1.5}\text{O}_{1.5}$. Green, purple, argenteous, and red balls represent Na, Mn, F, and O atoms, respectively. The corner-sharing octahedra are shown in purple.

TABLE I. The lattice constants, magnetic moments (m^{Mn}), energy difference (ΔE), and magnetic exchange coupling parameters (J_{ij}) of NaMnF_3 and oxygen-substituted NaMnF_3 ($\text{NaMnF}_{1.5}\text{O}_{1.5}$). The Neel (T_N) and Curie temperatures (T_C) of NaMnF_3 and $\text{NaMnF}_{1.5}\text{O}_{1.5}$ are listed, respectively. The Mn1, Mn2, Mn3, and Mn4 denote four locations of Mn atoms in NaMnF_3 , as well as in $\text{NaMnF}_{1.5}\text{O}_{1.5}$ crystal cell. The A, C, G, and F denote the total energy of A-type, C-type, G-type antiferromagnetic (AFM), and ferromagnetic (FM), respectively.

Composition	Lattice constants (Å)		m^{Mn} (μ_B/at)		ΔE (meV)		J_{ij} (meV)		T (K)
NaMnF ₃	a	5.72	Mn1	-4.675	A-G	54.631	J_1	-6.88	T_N (151)
	b	7.96	Mn2	4.675	C-G	23.097	J_2	-5.88	
	c	5.49	Mn3	4.675	F-G	78.611	J_3	-0.03	
			Mn4	-4.675					
NaMnF _{1.5} O _{1.5}	a	5.37	Mn1	3.298	A-F	169.977	J'_1	18.46	T_C (613)
	b	7.54	Mn2	3.338	C-F	159.366	J''_1	39.58	
	c	5.35	Mn3	4.476	G-F	306.014	J'''_1	0.73	
			Mn4	3.910		-			

As discussed above from Table I, the introduction of oxygen octahedra can regulate the magnetic ground state of NaMnF₃ effectively. Therefore, we first estimate magnetic exchange coupling parameters by utilizing an effective Heisenberg Hamiltonian [59,60]:

$$H = E_0 - \sum_{i \neq j} J_{ij} e_i \cdot e_j, \quad (4)$$

where E_0 denotes the nonmagnetic ground-state energy, e_i (e_j) denotes the unit vector along the direction of the magnetization at site i (j), and J_{ij} are exchange coupling parameters. The considered spin orderings for NaMnF₃ and NaMnF_{1.5}O_{1.5} are depicted in Fig. 2. Here, the nearest-neighbor (NN) interaction parameter J_1 , the next-nearest-neighbor (NNN) interaction parameter J_2 , and the third-nearest-neighbor (3-NN) interaction parameter J_3 are taken into account for NaMnF₃, as shown in Fig. 2(a). Based on the Eq. (4), the linear equations can be expressed as follows:

$$E_{\text{FM}} = E_0 - 4J_1 - 2J_2 - 8J_3$$

$$E_{\text{C-AFM}} = E_0 + 4J_1 - 2J_2 + 8J_3$$

$$\begin{aligned}
E_{A-A} &= E_0 - 4J_1 + 2J_2 + 8J_3 \\
E_{G-A} &= E_0 + 4J_1 + 2J_2 - 8J_3.
\end{aligned} \tag{5}$$

The antiferromagnetic transition temperature T_N can be estimated by mean-field approximation (MFA) [59,61]:

$$T_N = \frac{2}{3k_B}(-2J_1 - J_2 + 4J_3), \tag{6}$$

where k_B is the Boltzmann constant. From Eq. (5) and Eq. (6), the calculated results of J_{ij} are also listed in Table I, and $T_N = 151 \text{ K}$. The negative J_1 , J_2 , and J_3 indicate AFM interaction. Moreover, J_1 and J_2 are about 30 times larger than J_3 , demonstrating that J_1 and J_2 play a major role and thus results in G-AFM ground state. Given that the MFA overestimates the transition temperature due to the neglected effect of spin fluctuation [62], the 151 K of T_N is judged to be in quite good agreement with the experimental result [50,63].

We then estimate the Curie temperature T_C of the FM-state $\text{NaMnF}_{1.5}\text{O}_{1.5}$. As the environments around Mn1, Mn2, Mn3, and Mn4 are different due to the anion substitution, corresponding to the MnF_2O_4 , MnO_6 , MnF_6 , and MnF_4O_2 octahedra, respectively, in $\text{NaMnF}_{1.5}\text{O}_{1.5}$, for simplicity, three NN interactions between Mn atoms of different octahedra are considered as J'_1 (Mn1 and Mn2), J''_1 (Mn2 and Mn4), and J'''_1 (Mn2 and Mn3), respectively, as shown in Fig. 2(e). According to the Eq. (4), the linear equations are given as follows:

$$E_{\text{FM}} = E_0 - 4J'_1 - 2J''_1 - 8J'''_1$$

$$\begin{aligned}
E_{C-AFM} &= E_0 + 4J'_1 - 2J''_1 + 8J'''_1 \\
E_{A-A} &= E_0 - 4J'_1 + 2J''_1 + 8J'''_1 \\
E_{G-AFM} &= E_0 + 4J'_1 + 2J''_1 - 8J'''_1 ,
\end{aligned} \tag{7}$$

and similarly, the T_C can be estimated by MFA [59,61]:

$$T_C = \frac{2}{3k_B} (2J'_1 + J''_1 - 4J'''_1). \tag{8}$$

The calculation results indicate that J''_1 plays a crucial role in the high-temperature FM NaMnF_{1.5}O_{1.5} (see Table I).

To reveal the mechanism of the magnetic transition from AFM NaMnF₃ to FM NaMnF_{1.5}O_{1.5}, the projected density of states (PDOS), indicating stronger hybridization between O and Mn atoms in NaMnF_{1.5}O_{1.5}, are plotted in Fig. S5(a) and S5(b), and the spin configurations of Mn 3*d* orbitals in NaMnF_{1.5}O_{1.5} are also shown in Fig. S5(c). Compared with the pure Mn²⁺ in NaMnF₃, some of the Mn²⁺ are converted into Mn³⁺ in NaMnF_{1.5}O_{1.5}, resulting in the hybrid e_g of Mn²⁺ interacts with the empty orbital e_g of NN Mn³⁺ through O_{2*p*} orbital with a positive exchange coupling parameter. This double-exchange interaction [64] should be the origin for the FM feature of NaMnF_{1.5}O_{1.5}.

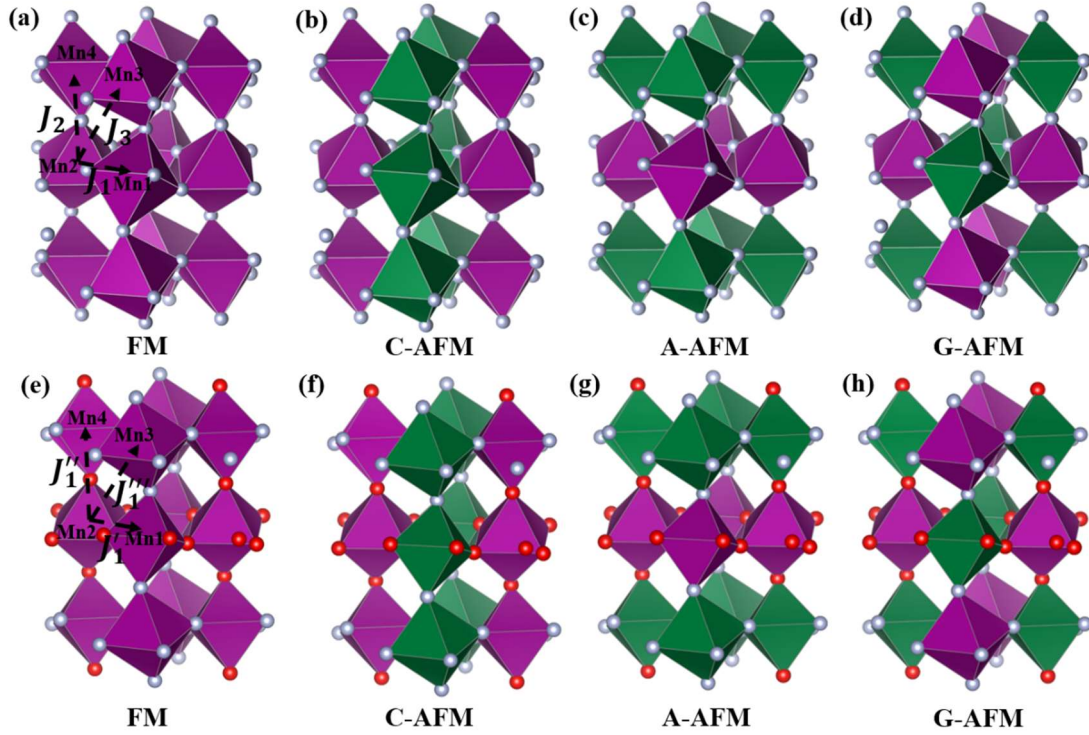


FIG. 2. Four considered magnetic configurations: (a) FM, (b) C-AFM, (c) A-AFM, (d) G-AFM of NaMnF_3 . Four considered magnetic configurations: (e) FM, (f) C-AFM, (g) A-AFM, (h) G-AFM of $\text{NaMnF}_{1.5}\text{O}_{1.5}$. The purple and green octahedra denote up and down spins of magnetic Mn atoms, respectively. The Mn1, Mn2, Mn3, and Mn4 denote four locations of Mn atoms in NaMnF_3 , as well as in $\text{NaMnF}_{1.5}\text{O}_{1.5}$ crystal cell. The exchange paths are indicated by black dashed arrows.

Strain engineering, as a promising way in manipulating the magnetism of transition metal compounds [46,65], providing an effective avenue to discover the novel magnetism of the ferromagnetic $\text{NaMnF}_{1.5}\text{O}_{1.5}$. Here, we define the strain as $\eta = \frac{d-d_0}{d_0}$, where d_0 and d correspond to the pristine and strained in-plane lattice constants, respectively. Thus, the positive value represents tensile strain and negative value represents compressive strain. Herein, large strains are taken into account based on previous experimental method [66]. Due to

the lowering effect of compressive strain on T_C (see Fig. S6 [47]), we only discuss the effect of tensile strain on the $\text{NaMnF}_{1.5}\text{O}_{1.5}$, within which structural stability can be kept (see Fig. S7 [47]). The calculations of noncollinear magnetism are performed to test whether the magnetic ordering orientations change under the tensile strain (see Fig. S8 [47]). By applying different in-plane biaxial tensile strains to the $\text{NaMnF}_{1.5}\text{O}_{1.5}$, we predict the changing trend of exchange coupling constants J_{ij} , as shown in Fig. 3(a). The result clearly shows that the exchange coupling constants J'_1 , J''_1 , and J'''_1 increase with the increase in biaxial tensile strain from 0 to 6%. However, as the larger tensile strain than 6% is applied, J'_1 and J'''_1 show an obvious decay, and even the sign of J'''_1 changes from positive to negative, which means the occurrence of the transition from FM interaction to AFM interaction. As can be seen from Fig. 3(a), J''_1 plays a major role in the magnetic interactions. Fig. 3(b) shows that the T_C can be strongly enhanced by the in-plane biaxial tensile strain from 613 K to 906 K in the strain range of 0 to 8%. As mentioned above, the MFA usually overestimates the transition temperature due to the neglected effect of spin fluctuation [62], and our calculated result T_N (151 K) presented above is 2.3 times of data from the experimental measurement [50,63]. This kind of correlation coefficient between the theoretical and experimental values was also used by the previous researches [61,67,68]. Thus, it can be expected that a

room temperature T_C might be achieved with tensile strain less than 8%. With larger tensile strain, the T_C shows a slow uptrend, which is the same trend as the major J_1'' .

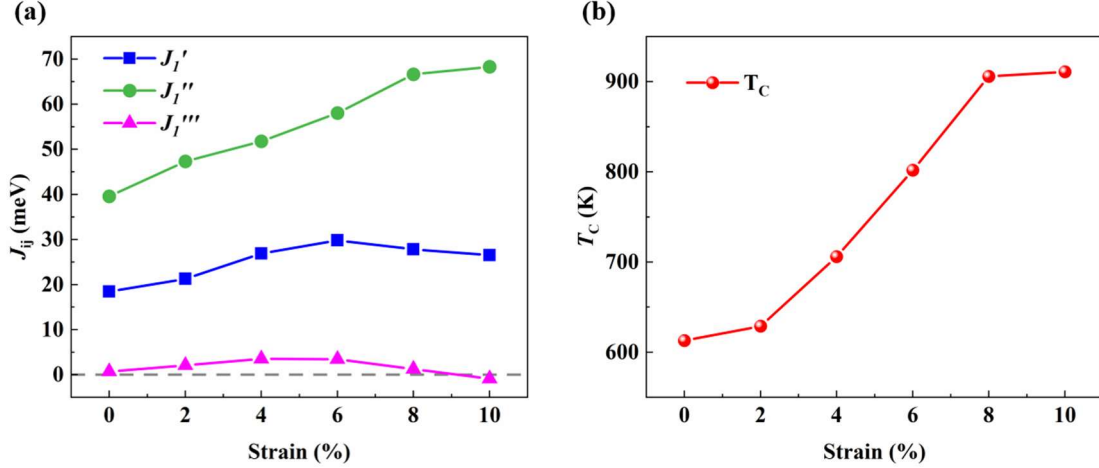


FIG. 3. (a) In-plane biaxial tensile strain dependencies of the magnetic-exchange interactions (J_{ij}). The gray horizontal dashed line denotes the boundary of magnetic interaction. (b) Evolution of Curie temperature (T_C) as a function of in-plane biaxial tensile strain.

To study the effect of in-plane biaxial tensile strain on structural distortions, we mainly focus on the oxygen-dominated octahedra, as shown in Fig. 4(a). It is generally believed that structural distortion of orthorhombic LaMnO_3 -like perovskite consists of octahedral rotation distortion and Jahn-Teller (JT) distortion, which can be evaluated from the deviation of magnetic-ion-ligand-magnetic-ion bond angles from 180° and the relative size of Mn-O bonds in oxygen octahedra, respectively. [69]. Figure 4(a) shows the in-plane Mn-O-Mn bond angles θ_1 and θ_2 , the out-of-plane Mn-O-Mn bond angle θ_3 , and the oxygen-dominated octahedra. As shown in Fig. 4(b), the θ_1 increases as the tensile strain

increases, while θ_2 reduces when the applied tensile strain exceeds 6%, thus on the whole, in-plane Mn-O-Mn bond angles increase with the increase of tensile strain, which means in-plane rotation distortion is suppressed. The θ_3 decreases as the tensile strain increases, indicating the out-of-plane rotation distortion is strengthened. Obvious changes in Mn-O-Mn bond angles indicate that rotation distortion of the oxygen-dominated octahedra contribute to the change in exchange interactions. The JT distortion, as an important role related to the structural distortions, is decomposed into the two normal modes: Q_2 and Q_3 . In order to evaluate the strength of each distortion mode, we define the $Q_2 = \frac{l_x - l_y}{\sqrt{2}}$ and $Q_3 = \frac{2l_z - l_x - l_y}{\sqrt{6}}$, where the l_x , l_y , and l_z denote the length of different Mn-O (Mn-F) bonds in oxygen-dominated octahedra, as shown in Fig. 4(a). Figures 4(c) and 4(d) show that the variation of Q_2 and Q_3 with tensile strain in fluorine-oxygen octahedron and oxygen octahedron, respectively. For the Q_2 -type JT distortion, it remains almost unchanged with the increase of tensile strain in both fluorine-oxygen octahedron and oxygen octahedron. While the Q_3 -type JT distortion is gradually enhanced with the increasing tensile strain in both octahedra. It should be noted that the value of Q_3 mode in an oxygen octahedron is about three times larger than that in the fluorine-oxygen octahedron, which suggests that the Q_3 -type JT distortion in the oxygen octahedron plays a major role in the change of exchange interactions. We attribute the

change of exchange interactions to the cooperative effect of rotation distortion and JT distortion.

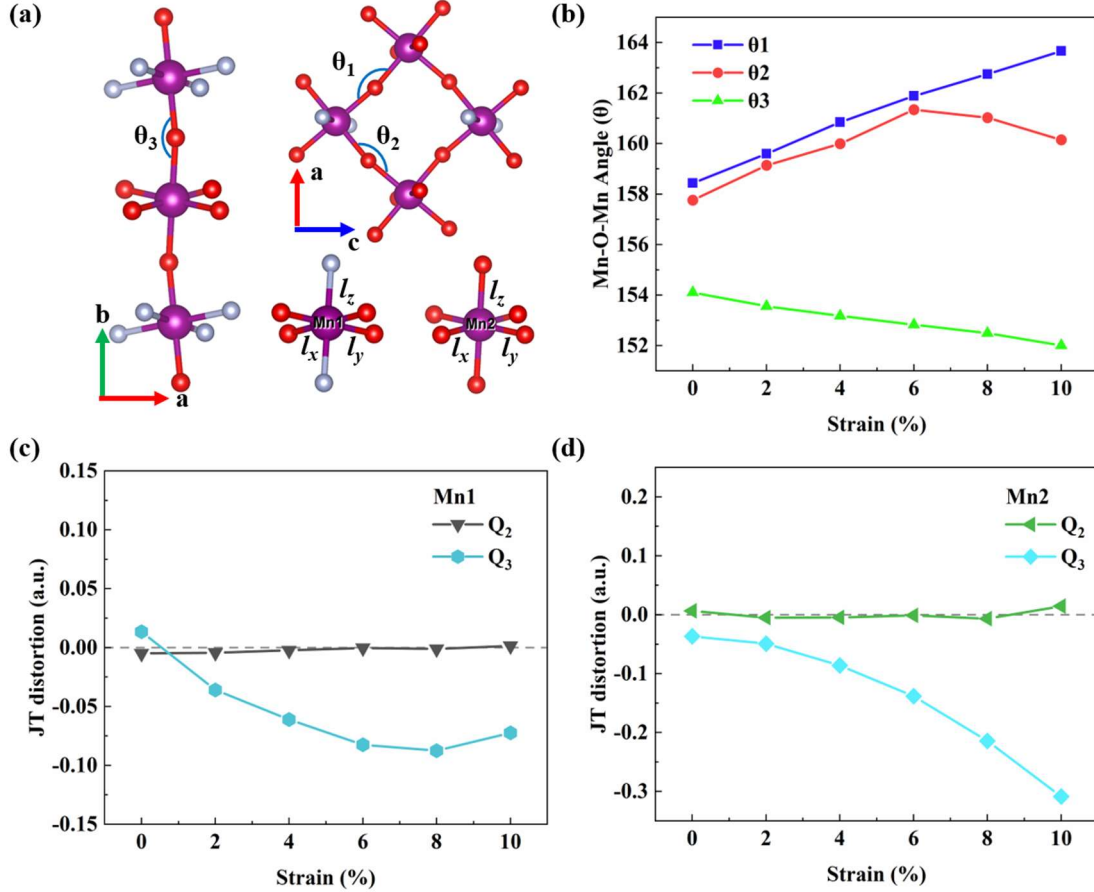


FIG. 4. (a) The Mn-O-Mn bond angles θ_1 and θ_2 from top view and θ_3 along b -axis. For the oxygen-dominated octahedra, the in-plane Mn-O bonds are denoted by l_x and l_y , and out-of-plane Mn-O bond is denoted by l_z . (b) Mn-O-Mn bond angles as a function of biaxial tensile strain. Evolution of the normal Jahn-Teller (JT) distortion mode (c) Q_2 and (d) Q_3 .

To understand the effect of biaxial tensile strain on the changing trends of exchange interactions, we calculated the total density of states (TDOS) of NaMnF_{1.5}O_{1.5} at zero strain and biaxial tensile strain of 10%, as shown in Fig. 5(a) and Fig. 5(b), respectively. One notable feature is

that the Fermi level only crosses the spin-up states without any strain, which means that the spin-up channel possesses metallic conductivity while the spin-down channel is semiconducting, indicating a half-metallic character, as shown in Fig. 5(a). Moreover, Fig. 5(a) shows that the spin-flip excitation energy (Δ_{sf}) is equal to the spin-down gap (Δ_{\downarrow}) at zero strain. When a large tensile strain ($\eta = 10\%$) is applied, the Δ_{sf} and Δ_{\downarrow} increase from 1.91 eV to 2.72 eV and 2.84 eV, respectively, as shown in Fig. 5(b). The enhanced spin polarization increases the spin transport distance, which indicates that the strain-tuned $\text{NaMnF}_{1.5}\text{O}_{1.5}$ is a potential candidate for spintronic materials. As shown in Fig. 5(c), the schematic electronic structures restructuring illustrates the regulation mechanism more visually.

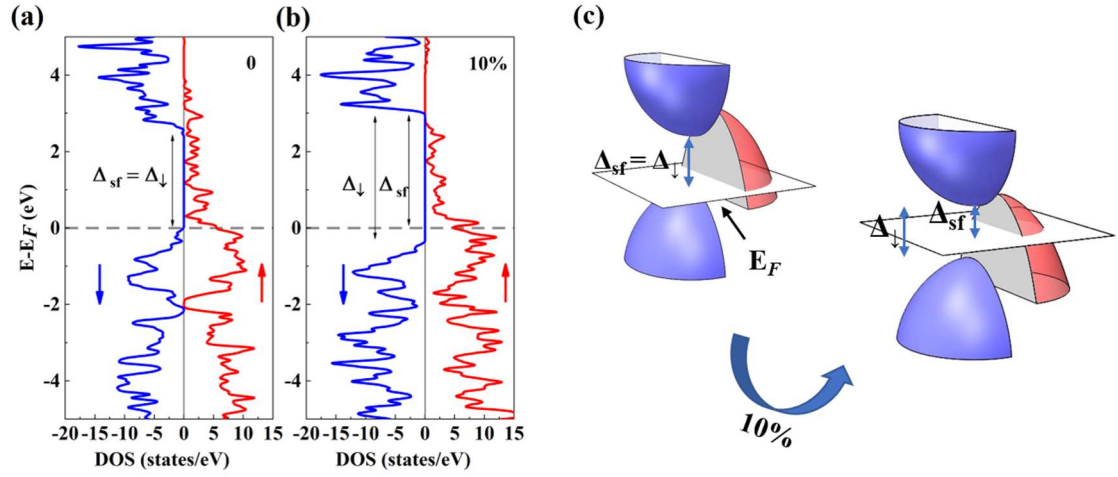


FIG. 5. The total density of states (TDOS) of $\text{NaMnF}_{1.5}\text{O}_{1.5}$ at (a) 0 strain and (b) biaxial tensile strain of 10%. The symbols Δ_{sf} and Δ_{\downarrow} represent the spin-flip excitation energy and spin-down gap, respectively. The Fermi level is set at zero. (c) The schematic of the electronic structures restructuring models at zero strain and biaxial tensile strain of 10%. The white plane denotes the Fermi surface. Spin-up and spin-down states are marked by red and blue, respectively.

We then investigated the PDOS on the Mn-3*d* orbitals in MnO₆ octahedra (Mn²⁺) at various biaxial tensile strain, as shown in Figs. 6(a)-6(f). For comparison, Fig. S9 [47] shows that the *t*_{2*g*} orbitals change slightly with the increased biaxial tensile strain. According to the previous study [65,70], the *e*_{*g*} (*d*_{*z*²}/*d*_{*x*²-*y*²}) exchange interactions are FM and mainly determine the interplanar exchange. As mentioned above, the *Q*₃-type JT distortion of the oxygen octahedra gradually promotes as the applied biaxial tensile strain increases (see Fig. 4(d)), which enhanced the crystal field splitting. Further results can be seen from Figs. 6(a)-6(f), the tensile strain increases the orbital overlap between *d*_{*z*²} and *d*_{*x*²-*y*²}, implying the FM *e*_{*g*} - *e*_{*g*} exchange interaction is enhanced, which explains the increase of the interplanar exchange coupling constant *J*₁^{''} with increasing biaxial tensile strain (see Fig. 3(a)). Furthermore, the bond-angle-related rotation distortion is considered. According to the Goodenough-Kanamori-Anderson rules, the super-exchange interaction favors AFM with 180° Mn-O-Mn bond angle [71-73]. The out-of-plane Mn-O-Mn bond angle θ_3 decreases monotonically with the increase of the biaxial tensile strains, as shown in Fig. 4(b), indicating the AFM interaction lessens, which also links the rotation distortion to the changing trend of the major exchange coupling constant *J*₁^{''} (see Fig. 3(a)). However, previous study confirmed that the *d*_{*z*²}-*d*_{*z*²} FM exchange determine the changing trend of the intraplane exchange and is strongly

affected by the in-plane Mn-O-Mn bond angle [65]. As shown in Figs. 6(a)-6(c), the intensity of the projected orbital d_{z^2} changes slightly at the smaller biaxial tensile strain (0-4%). As the tensile strain increases, in-plane Mn-O-Mn bond angle θ_2 gradually decreases and the intensity of the projected orbital d_{z^2} increases obviously, indicating that the bandwidth of the d_{z^2} decreases and the in-plane orbital overlaps between the d_{z^2} states reduce. These results further lead to the reduction of the in-plane FM exchange coupling constant J'_1 (see Fig. 3(a)).

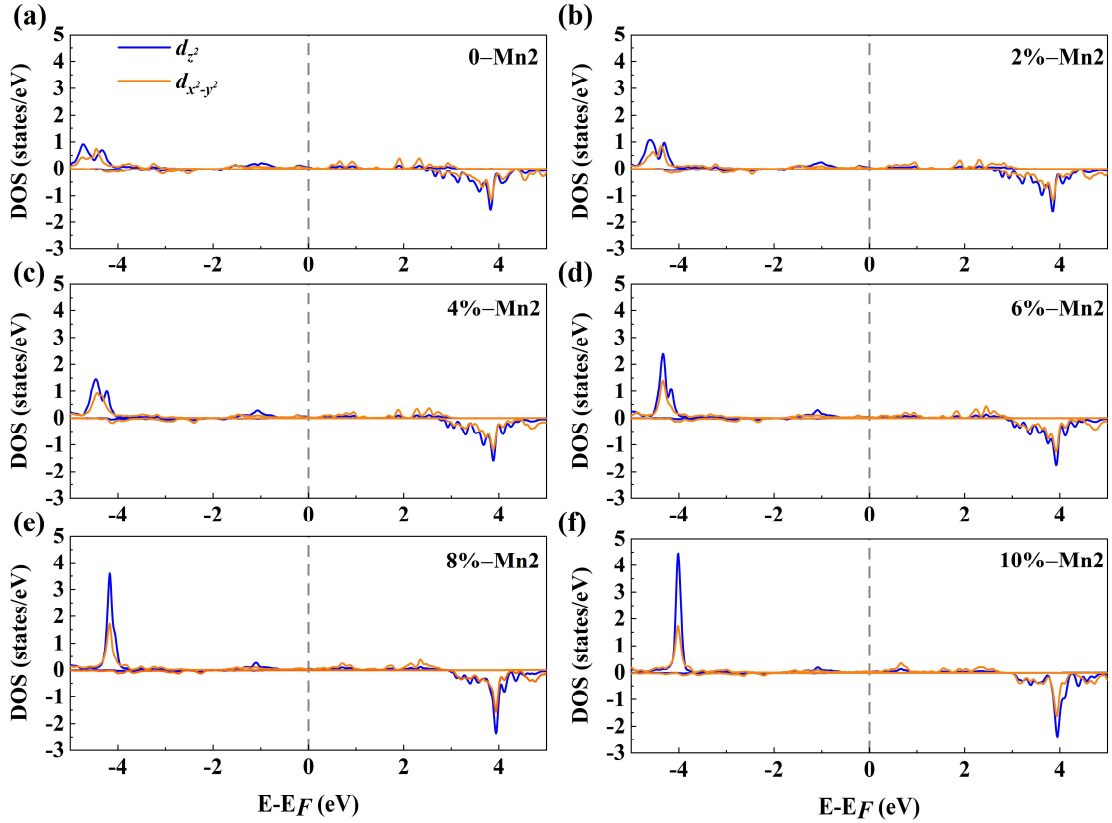


FIG. 6. The projected density of states (PDOS) on the Mn-3d orbitals in MnO₆ octahedra (Mn2) at (a) 0 strain, biaxial tensile strain (b) 2%, (c) 4%, (d) 6%, (e) 8%, and (f) 10%. The gray perpendicular dashed lines denote the Fermi level.

IV. CONCLUSIONS

In conclusion, we theoretically investigated the structural, magnetic, and electronic properties of oxygen-substituted NaMnF_3 under biaxial tensile strain by the first-principles approaches. We selected the simpler structure containing an oxygen octahedron to explore the underlying physical mechanism, which demonstrates that the introduced oxygen octahedra induce a transition from the intrinsic G-AFM NaMnF_3 to the high-temperature FM $\text{NaMnF}_{1.5}\text{O}_{1.5}$. Moreover, the interesting transition from an insulator to a half-metal makes it possible in spintronic applications. By applying the in-plane biaxial tensile strain, the T_C increases significantly, and a room temperature T_C may be expected. The changing trends of exchange coupling constants with the increasing of biaxial tensile strain can be attributed to the cooperative effects of Jahn-Teller distortion and rotation distortion. Our work may provide a new angle in designing novel high-temperature ferromagnets for the future theoretical and experimental works, and the coexisting half-metallic behavior suggests potential application in new spintronic devices.

ACKNOWLEDGMENTS

This work is supported by the National Key Basic Research Program of China (Grant Nos. 2019YFA0308500 and 2020YFA0309100), the

National Natural Science Foundation of China (Grant Nos. 11721404, 51761145104, 11974390, and 11674385), the Key Research Program of Frontier Sciences of the Chinese Academy of Sciences (Grant No. QYZDJ-SSW-SLH020), the Youth Innovation Promotion Association of the Chinese Academy of Sciences (Grant No. 2018008), the Beijing Nova Program of Science and Technology (Grant No. Z191100001119112), Beijing Natural Science Foundation (2202060), and the Strategic Priority Research Program (B) of the Chinese Academy of Sciences (Grant No. XDB33030200).

- [1] Z. B. G. Y. W. Du, J. S. Zhu, H. Huang, W. P. Ding, and D. Feng, *Phys. Rev. Lett.* **78**, 1142 (1997).
- [2] R. E. Cohen, *Nature* **358**, 135 (1992).
- [3] C. Ma, K.-j. Jin, C. Ge, and G.-z. Yang, *Phys. Rev. B* **97**, 115103 (2018).
- [4] M. Fiebig, T. Lottermoser, D. Meier, and M. Trassin, *Nat. Rev. Mater.* **1**, 16046 (2016).
- [5] X. He and K.-j. Jin, *Phys. Rev. B* **93**, 161108 (2016).
- [6] R. M. Dubrovin, L. N. Alyabyeva, N. V. Siverin, B. P. Gorshunov, N. N. Novikova, K. N. Boldyrev, and R. V. Pisarev, *Phys. Rev. B* **101**, 180403 (2020).
- [7] Gotthard Sági-Szabó, Ronald E. Cohen, and Henry Krakauer, *Phys. Rev. Lett.* **80**, 4321 (1998).
- [8] Y. Maeno, H. Hashimoto, K. Yoshida, S. Nishizaki, T. Fujita, J. G. Bednorz, and F. Lichtenberg, *Nature* **372**, 532 (1994).
- [9] K.-j. Jin, H.-b. Lu, Q.-l. Zhou, K. Zhao, B.-l. Cheng, Z.-h. Chen, Y.-l. Zhou, and G.-Z. Yang, *Phys. Rev. B* **71**, 184428 (2005).
- [10] M. Imada, A. Fujimori, and Y. Tokura, *Rev. Mod. Phys.* **70**, 1039 (1998).
- [11] E. Dagotto, *Science* **309**, 257 (2005).
- [12] E. Dagotto, T. Hotta, and A. Moreo, *Phys. Rep.* **344**, 1 (2001).
- [13] Y. S. Hou, H. J. Xiang, and X. G. Gong, *Phys. Rev. B* **89**, 064415 (2014).
- [14] T.-C. Sum and N. Mathews, *Halide Perovskites: Photovoltaics, Light Emitting Devices, and Beyond* (Wiley-VCH, Weinheim 2019).
- [15] R. Hu, C. Li, X. Wang, T. Zhou, X. Yang, G. Gao, and Y. Zhang, *Catal. Commun.* **40**, 71 (2013).

- [16] H. Yusa, Y. Shirako, M. Akaogi, H. Kojitani, N. Hirao, Y. Ohishi, and T. Kikegawa, *Inorg. Chem.* **51**, 6559 (2012).
- [17] D. P. Dobson, S. A. Hunt, A. Lindsay-Scott, and I. G. Wood, *Phys. Earth Planet. Inter.* **189**, 171 (2011).
- [18] L. Clark and P. Lightfoot, in *Photonic and Electronic Properties of Fluoride Materials Elsevier, Amsterdam* (2016), pp. 261.
- [19] R. M. Dubrovin, S. A. Kizhaev, P. P. Syrnikov, J. Y. Gesland, and R. V. Pisarev, *Phys. Rev. B* **98**, 060403 (2018).
- [20] A. C. Garcia-Castro, A. H. Romero, and E. Bousquet, *Phys. Rev. B* **90**, 064113 (2014).
- [21] A. C. Garcia-Castro, N. A. Spaldin, A. H. Romero, and E. Bousquet, *Phys. Rev. B* **89**, 104107 (2014).
- [22] M. Yang, A. Kc, A. C. Garcia-Castro, P. Borisov, E. Bousquet, D. Lederman, A. H. Romero, and C. Cen, *Sci. Rep.* **7**, 7182 (2017).
- [23] A. Kc, P. Borisov, V. V. Shvartsman, and D. Lederman, *Appl. Phys. Lett.* **110** 092901 (2017).
- [24] N. Manyala, Y. Sidis, J. F. DiTusa, G. Aeppli, D.P. Young, and Z. Fisk, *Nature* **404**, 581 (2000).
- [25] A. Chernyshov, M. Overby, X. Liu, J. K. Furdyna, Y. Lyanda-Geller, and L. P. Rokhinson, *Nat. Phys.* **5**, 656 (2009).
- [26] J. M. D. Coey and S. Sanvito, *J. Phys. D: Appl. Phys.* **37**, 988 (2004).
- [27] R. A. de Groot, F. M. Mueller, P. G. v. Engen, and K. H. J. Buschow, *Phys. Rev. Lett.* **50**, 2024 (1983).
- [28] J.-H. Park, E. Vescovo, H.-J. Kim, C. Kwon, R. Ramesh, and T. Venkatesan, *Nature* **392**, 794 (1998).
- [29] X. F. Zhai, L. Cheng, Y. Liu, C. M. Schlepuetz, S. Dong, H. Li, X. Q. Zhang, S. Q. Chu, L. R. Zheng, J. Zhang, A. D. Zhao, H. Hong, A. Bhattacharya, J. N. Eckstein, and C. G. Zeng, *Nat. Commun.* **5**, 4283 (2014).
- [30] J. He, A. Borisevich, S. V. Kalinin, S. J. Pennycook, and S. T. Pantelides, *Phys. Rev. Lett* **105**, 227203 (2010).
- [31] A. M. GLAZER, *Acta Crystallogr., B* **28**, 3384 (1972).
- [32] P. Zubko, S. Gariglio, M. Gabay, P. Ghosez, and J.-M. Triscone, *Annu. Rev. Condens. Matter Phys.* **2**, 141 (2011).
- [33] W. N. Ren, K. J. Jin, J. S. Wang, C. Ge, E. J. Guo, C. Ma, C. Wang, and X. Xu, *Sci. Rep.* **11**, 2744 (2021).
- [34] Y.-H. Chu, L. W. Martin, M. B. Holcomb, and R. Ramesh, *Mater. Today* **10**, 16 (2007).
- [35] H. Banerjee, O. Janson, K. Held, and T. Saha-Dasgupta, *Phys. Rev. B* **100**, 115143 (2019).
- [36] J. S. White, M. Bator, Y. Hu, H. Luetkens, J. Stahn, S. Capelli, S. Das, M. Dobeli, Th. Lippert, V. K. Malik, J. Martyniczuk, A. Wokaun, M. Kenzelmann, Ch. Niedermayer, and C. W. Schneider, *Phys. Rev. Lett.* **111**, 037201 (2013).
- [37] C. Tassel, Y. Kuno, Y. Goto, T. Yamamoto, C. M. Brown, J. Hester, K. Fujita, M. Higashi, R. Abe, K. Tanaka, Y. Kobayashi, and H. Kageyama, *Angew. Chem.* **54**,

- 516 (2015).
- [38] K. Liu, Y. Hou, X. Gong, and H. Xiang, *Sci. Rep.* **6**, 19653 (2016).
- [39] D. Oka, Y. Hirose, H. Kamisaka, T. Fukumura, K. Sasa, S. Ishii, H. Matsuzaki, Y. Sato, Y. Ikuhara, and T. Hasegawa, *Sci. Rep.* **4**, 4987 (2014).
- [40] Y. Kurauchi, T. Katayama, A. Chikamatsu, and T. Hasegawa, *J. Phys. Chem. C* **123**, 31190 (2019).
- [41] J. F. G. Kresse and J. Furthmüller, *Phys. Rev. B* **54**, 11169 (1996).
- [42] J. F. G. Kresse and J. Furthmüller, *Comput. Mater. Sci.* **6**, 15 (1996).
- [43] P. E. Blochl, *Phys. Rev. B* **50**, 17953 (1994).
- [44] J. P. Perdew, A. Ruzsinszky, G. I. Csonka, O. A. Vydrov, G. E. Scuseria, L. A. Constantin, X. Zhou, and K. Burke, *Phys. Rev. Lett.* **100**, 136406 (2008).
- [45] A. I. Liechtenstein, V. V. Anisimov, and J. Zaanen, *Phys. Rev. B* **52**, R5467 (1995).
- [46] A. C. Garcia-Castro, A. H. Romero, and E. Bousquet, *Phys. Rev. Lett.* **116**, 117202 (2016).
- [47] See Supplemental Material for complementary Figs. S1-S9: The effective on-site Coulomb energy U_{eff} dependence of magnetic ground state for NaMnF₃ and NaMnF_{1.5}O_{1.5}; The effective on-site Coulomb energy U_{eff} dependence of lattice constants for NaMnF₃ and NaMnF_{1.5}O_{1.5}; Four structures based on different positions of MnO₆ octahedron in NaMnF_{1.5}O_{1.5}; The DOS of four structures based on different positions of MnO₆ octahedron in NaMnF_{1.5}O_{1.5}; The orbital occupation and spin configuration of Mn ions in NaMnF_{1.5}O_{1.5}; The compressive strains dependence of exchange coupling constants J_{ij} and Curie temperature T_C for NaMnF_{1.5}O_{1.5}; The tensile strains dependence of formation energy for NaMnF_{1.5}O_{1.5}; The tensile strain dependence of magnetic ordering orientations for different magnetic states; The projected t_{2g} orbitals at the various biaxial tensile strains for NaMnF_{1.5}O_{1.5}.
- [48] K. Momma and F. Izumi, *J. Appl. Crystallogr.* **44**, 1272 (2011).
- [49] Alicja Ratuszna, Katarzyna Majewska, and Tadeusz Lis, *Acta Crystallogr., Sect. C: Cryst. Struct. Commun.* **45**, 548 (1989).
- [50] P. Daniel, M. Rousseau, A. Desert, A. Ratuszna, and F. Ganot, *Phys. Rev. B* **51**, 12337 (1995).
- [51] J. F. Scott and R. Blinc, *J Phys.: Condens. Matter* **23**, 113202 (2011).
- [52] C. Freysoldt, B. Grabowski, T. Hickel, J. Neugebauer, G. Kresse, A. Janotti, and C. G. Van de Walle, *Rev. Mod. Phys.* **86**, 253 (2014).
- [53] W. Chen, X. Hou, X. Shi, and H. Pan, *ACS Appl. Mater. Interfaces* **10**, 35289 (2018).
- [54] T. Roy, D. Pandey, and A. Chakrabarti, *Phys. Rev. B* **93** (2016).
- [55] X. Zhang, Y. Cui, L. Sun, M. Li, J. Du, and Y. Huang, *J. Mater. Chem. C* **7**, 13203 (2019).
- [56] D. Chen, X. Lei, Y. Wang, S. Zhong, G. Liu, B. Xu, and C. Ouyang, *Appl. Surf. Sci.* **497** 143809 (2019).
- [57] V. M. Goldschmidt, *Naturwissenschaften* **14**, 477 (1926).
- [58] A. Hoffmann, *Zeitschrift Fur Physikalische Chemie-Abteilung B-Chemie Der*

- Elementarprozesse Aufbau Der Materie **28**, 65 (1935).
- [59] A.I. Liechtenstein, M.I. Katsnelson, V.P. Antropov and V.A. Gubanov, *J. Magn. Magn. Mater.* **67**, 65 (1987).
- [60] Y. Fang, S. Wu, Z.-Z. Zhu, and G.-Y. Guo, *Phys. Rev. B* **98**, 125416 (2018).
- [61] M. Toyoda, K. Yamauchi, and T. Oguchi, *Phys. Rev. B* **87**, 224430 (2013).
- [62] P. Baettig, C. Ederer, and N. A. Spaldin, *Phys. Rev. B* **72**, 214105 (2005).
- [63] A. Katrusiak. and A. Ratuszna, *Solid State Commun.* **84**, 435 (1992).
- [64] C. Zener, *Phys. Rev.* **82**, 403 (1951).
- [65] J. Zhang, C. Ji, Y. Shangguan, B. Guo, J. Wang, F. Huang, X. Lu, and J. Zhu, *Phys. Rev. B* **98**, 195133 (2018).
- [66] M. G. Seung Sae Hong, Manish Verma, Varun Harbola, Bai Yang Wang, Di Lu, Arturas Vailionis, Yasuyuki Hikita, Rossitza Pentcheva, James M. Rondinelli, Harold Y. Hwang, *Science* **368**, 71 (2020).
- [67] M. Liu, C.-E. Hu, C. Cheng, and X. Chen, *J. Phys. Chem. C* **122**, 1946 (2018).
- [68] H. Liu, J. T. Sun, M. Liu, and S. Meng, *J. Phys. Chem. Lett.* **9**, 6709 (2018).
- [69] C. Ji, Wang, Yancheng, Guo, Bixiang, Shen, Xiaofan, Luo, Qunyong, Wang, Jianli, Meng, Xianwen, Zhang, Junting, Lu, Xiaomei, Zhu, Jinsong, *Phys. Rev. B* **100**, 174417 (2019).
- [70] N. H. Igor Solovyev, and Kiyoyuki Terakura, *Phys. Rev. Lett.* **76**, 4825 (1996).
- [71] J. B. Goodenough, *Phys. Rev.* **100**, 564 (1955).
- [72] J. B. Goodenough, *J. Phys. Chem. Solids* **6**, 287 (1958).
- [73] J. Kanamori, *J. Phys. Chem. Solids* **10**, 87 (1959).